

See discussions, stats, and author profiles for this publication at: <https://www.researchgate.net/publication/282567309>

article

DATASET · OCTOBER 2015

READS

21

7 AUTHORS, INCLUDING:



[Grzegorz Zajac](#)

Jagiellonian University

6 PUBLICATIONS 2 CITATIONS

SEE PROFILE



[Szymon Buda](#)

Jagiellonian University

12 PUBLICATIONS 12 CITATIONS

SEE PROFILE



[Jadwiga Frelek](#)

Polish Academy of Sciences

130 PUBLICATIONS 1,281 CITATIONS

SEE PROFILE



[Malgorzata Baranska](#)

Jagiellonian University

159 PUBLICATIONS 1,866 CITATIONS

SEE PROFILE

Prediction of ROA and ECD Related to Conformational Changes of Astaxanthin Enantiomers

Grzegorz Zajac,^{†,‡} Agnieszka Kaczor,^{†,‡} Szymon Buda,[†] Jacek Młynarski,^{†,§} Jadwiga Frelek,[§] Jan Cz. Dobrowolski,^{||,⊥} and Małgorzata Baranska^{*,†,‡}

[†]Faculty of Chemistry, Jagiellonian University, 3 Ingardena Str., 30-060 Krakow, Poland

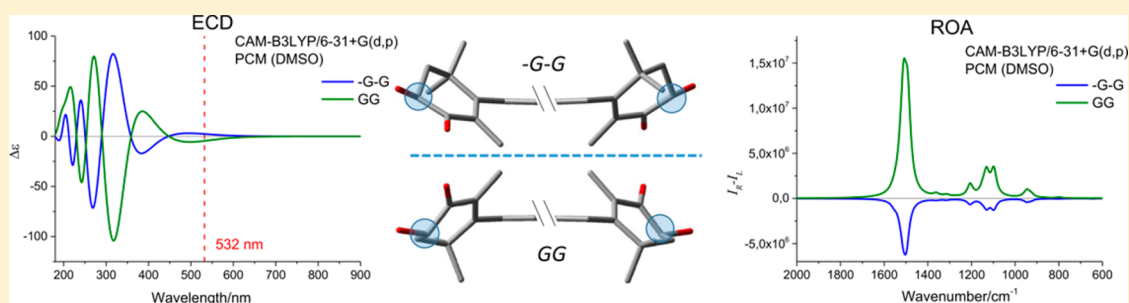
[‡]Jagiellonian Centre for Experimental Therapeutics (JCET), Jagiellonian University, 14 Bobrzyńskiego Str., 30-348 Krakow, Poland

[§]Institute of Organic Chemistry, Polish Academy of Sciences, Kasprzaka 44/52, 01-224 Warsaw, Poland

^{||}National Medicines Institute, 30/34 Chełmska Str., 00-725 Warsaw, Poland

[⊥]Institute of Nuclear Chemistry and Technology, 16 Dorodna Str., 03-195 Warsaw, Poland

Supporting Information



ABSTRACT: ECD, ROA, and VCD were used to characterize astaxanthin conformers that differ in their arrangements of the β -ionone ring in respect to the chain. We obtained ECD spectra experimentally, and the ECD, ROA, and VCD spectra of both individual conformers and conformation-averaged mixtures were predicted using quantum-chemical calculations at the CAM-B3LYP level of theory using the PCM solvation model. The chiroptical methods employed (particularly ECD and ROA) were considerably more sensitive to conformational changes of astaxanthin compared to “mono-signed” conventional Raman spectroscopy. Strikingly, conformers that are the same optical isomers (e.g., of 3S,3'S-astaxanthin), while geometrically nearly mirror images, exhibited sign-inversed ECD and ROA spectra. The conformational sensitivity of these chiroptical methods makes them a promising tool in the study of carotenoids in the natural environment (for instance, in *de novo* algal or yeast astaxanthin sources).

1. INTRODUCTION

Astaxanthin (3,3'-dihydroxy- β,β -carotene-4,4'-dione, AXT) exhibits a variety of configurations related to geometry (all-*E* (all-*trans*) and *Z* isomers (*cis*-forms)), conformation, and stereoisomerism (3*R*,3'*R*-, 3*S*,3'*S*-, and *meso*-AXT). The natural occurrence and biological activity of AXT conformers is diverse, yet it is not very well understood and still a subject of a debate.^{1,2}

The enantiomeric and *meso*- forms have been found in numerous species of aquatic animals, where AXT occurs as a specific optical isomer or a mixture of them.^{3,4} (3*S*,3'*S*)-AXT can be detected in some fish (salmonids),⁵ birds, bacteria, and less frequently in higher plants, including as a major carotenoid in some of them, e.g., in flowers of *Adonis* spp.⁶ In green algae, AXT frequently occurs as a secondary carotenoid, yet in *Haematococcus pluvialis*^{7,8} its concentration is so high that the species is commercially used as a source of astaxanthin. In contrast, the (3*R*,3'*R*)-AXT isomer is the major carotenoid present in *Phaffia rhodozyma* (*Xanthophyllomyces dendrorhous*) red yeast.⁹

AXT isomers show different bioavailability. For instance, the *Salmo salar* and *Salvelinus alpinus* fish species, when fed with the *E/Z* AXT mixture, selectively accumulate the all-*E* astaxanthin in plasma, muscle, and intestinal tissues and the 13-*Z*-astaxanthin isomer in liver.^{5,10} More recently, it has been found that in fish tissues the *E*- and *Z*-isomer ratio is highest in salmon gonads (82:18) and lowest in herring gonads (24:76).¹¹ However, no selectivity for astaxanthin *R/S* isomers has been detected in trout or human plasma.^{5,12} Furthermore, administering a mixture of geometrical and optical isomers has indicated that a selective process increases the *Z* to all-*E* isomer ratio compared to that before the uptake in blood, and that the (3*R*,3'*R*)-astaxanthin isomer is selectively accumulated in blood plasma: ca. 55% after the uptake versus ca. 30% in the administered dose.¹³

Received: July 24, 2015

Revised: August 25, 2015

Published: August 25, 2015

It is well-known that astaxanthin is a potent antioxidant.^{14,15} Nevertheless, it has recently been demonstrated that 9-*Z* astaxanthin has a much higher antioxidant potency than the all-*E* isomer.¹⁶ Moreover, a mixture of astaxanthin *E/Z* isomers appeared to be a better antioxidant in vitro than the all-*E* astaxanthin in model experiments with cod liver oil and fatty acid ethyl esters enriched in eicosapentaenoic and docosahexanoic acids.¹⁷

AXT is a nonrigid molecule exhibiting strong Raman resonance enhancement in the visible range. Its chiroptical properties can be studied by electron circular dichroism (ECD) and by vibrational optical activity (VOA) spectroscopies: Raman optical activity (ROA) and vibrational circular dichroism (VCD). The ROA spectroscopy is suitable for this purpose because of possible resonance enhancement.¹⁸ AXT is a homodichiral carotenoid, i.e., ending with two identical chiral groups affecting the molecule independently, yet, in some respects, additively. The ECD spectrum of (3*S*,3'*S*)-AXT in CH₂Cl₂ solution shows a series of strong bands of alternating sign in the UV region.^{19,20} For 3*S*,3'*S*-15-*Z*-astaxanthin, the signs of some ECD maxima appear to be opposite to those of the all-*E* isomer.²⁰

Electronic and Raman spectra of carotenoids may exhibit strong temperature dependence.^{21–24} The molar electronic circular dichroism ($\Delta\epsilon$) intensities may also increase significantly after cooling the samples to liquid nitrogen temperature (–195.8 °C), but as the temperature is lowered, the CD bands of astaxanthin can even change their sign.²⁵

We have previously shown²⁶ that for a given enantiomer (the most stable conformation of the end groups and the all-*E* geometry of the polyene chain are assumed to be constant), the AXT exhibits nine conformers resulting from mutual orientation of the end rings: *GG*, *-GG*, *-G-G*, *GT*, *T-G*, *TT*, *G-G*, *TG*, and *-GT* (*G*-, *gauche*; *T*-, *trans* conformations). Of these, three are energetically degenerated because rotation about the C₂ axis perpendicular to the polyene chain converts one into another: *-GG* = *G-G*, *GT* = *TG*, and *T-G* = *-GT*.²⁶ For the six different AXT conformers, the ROA spectra were calculated with the B3LYP and M05 functionals in the gas phase.²⁷ It has been found that some of the AXT conformers exhibit different signs of the bands than other conformers. As a result, the conformer population averaged spectrum of astaxanthin can exhibit both signs of the bands or be monosigned depending on which conformers are dominant. Moreover, using different basis sets or density functional theory (DFT) functionals results in different conformer populations, thus yielding either a monosigned ROA spectrum or a spectrum displaying bands of both signs.²⁷

In light of the impact of geometry and chirality on astaxanthin bioavailability, these properties are studied using methods that allow for the selective and sensitive determination of AXT conformation(s) and optical isomerism(s). Previously, we discussed only the ROA spectra of the six stable AXT conformers calculated with the B3LYP and M05 functionals in the gas phase.²⁷ In this study, we use the combination of ECD, ROA, (in some respect) VCD, quantum-chemical calculations at the CAM-B3LYP level, and the PCM model to explain the impact of the AXT conformation on its chiroptical properties. The vibrational optical activity of AXT is low in intensity and can hardly be observed experimentally, but we recorded the ECD spectra of the two AXT enantiomers. To benefit most from the experimental data, we used quantum-chemical calculations to support the analysis of the spectra. We predicted the ECD spectra of all conformers and juxtaposed them with the corresponding ROA ones by applying DFT methods and

a PCM environment. The relation between the signs of the ROA spectra and the ECD band closest to the excitation wavelength used in ROA calculations will be discussed.

2. EXPERIMENTAL SECTION

2.1. Separation of AXT Enantiomers. Racemic astaxanthin (Scheme 1) was obtained from BASF. Astaxanthin enantiomers were separated using column chromatography after di(–)-camphanic ester derivatization.²⁸ The separation and purity of astaxanthin–di(–)-camphanat esters as well as the *E–Z* isomerization after saponification of the AXT enantiomer esters were examined by HPLC.

2.2. ECD Spectra of Enantiomers. The experimental ECD spectra of both enantiomers of astaxanthin were recorded using a Jasco J-815 spectrometer at room temperature in spectroscopic grade DMSO. Solutions with a concentration of $\sim 3 \times 10^{-6}$ M were measured in a quartz cell with a path length of 1 and 2 cm in the 250–800 nm spectral range. All spectra were recorded using a scanning speed of 100 nm min^{–1}, a step size of 0.2 nm, a bandwidth of 1 nm, a response time of 0.5 s, and an accumulation of five scans. The spectra were background-corrected using spectra of DMSO recorded under the same conditions.

2.3. Calculations. Geometry optimizations, harmonic frequencies and ROA and VCD intensities of the six most stable all-*E* isomer of 3*S*,3'*S*-astaxanthin conformers (*GG*, *-GG*, *-G-G*, *GT*, *T-G*, and *TT*)²⁶ in the gas phase, and DMSO solution were calculated using the CAM-B3LYP²⁹ DFT functional combined with the 6-31+G(d,p) basis set. Additionally, two previously used functionals were tested, B3LYP^{30,31} and M05,³² but now in the PCM environment. The CAM-B3LYP functional contains the long-range correction to B3LYP and has been shown to predict C–C and C=C distances, polarizabilities of long chains, and electronic excitations much better than B3LYP.³³ It also improves reproduction of the oscillator strengths compared to that in both the B3LYP and M05 functionals.³⁴ Moreover, for different ECD transition types, the CAM-B3LYP functional exhibits a good agreement with the sophisticated RICC2 method (coupled cluster with approximate singles and doubles method and resolution of identity approximation).³⁵ In some studies, CAM-B3LYP yielded the most accurate excitation energies and intensities.³⁶ The solvation model was applied to account for the influence of the DMSO surrounding the integral equation formalism polarizable continuum model (IEF-PCM).³⁷ The excitation energies for the first 40 singlet excitation states and the rotatory strengths were calculated using the time-dependent density functional theory (TD-DFT) approach for both the gas phase and the IEF-PCM simulated DMSO solution. The ECD curves were obtained by using Gaussian functions of the 0.2 eV half width. The averaged spectra were calculated based on the free Gibbs energies and the Boltzmann distribution at 298 K. No imaginary frequency was present in the optimized structures. All calculations were performed using the Gaussian 09 suite of programs.³⁸

3. RESULTS AND DISCUSSION

3.1. UV–Vis and ECD Spectra of AXT Enantiomers. The all-*E* configuration of the conjugated polyene chain in AXT establishes good conditions for π -electron delocalization and constitutes a chromophore yielding a characteristic UV–vis pattern. Nevertheless, in the first approximation, the UV–vis spectrum only provides information about the chromophore,

Scheme 1. Astaxanthin Structural Formula and Scheme of Separation of AXT Enantiomers

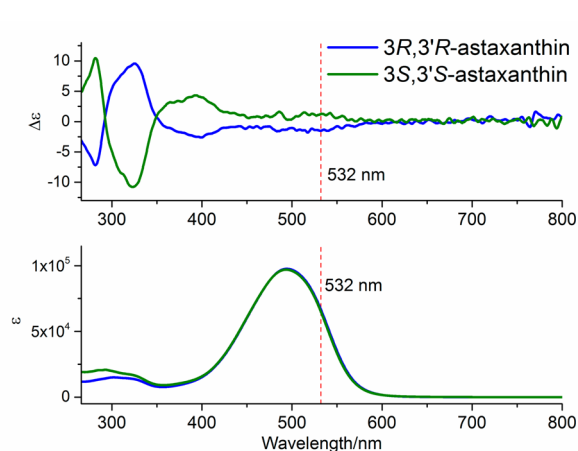
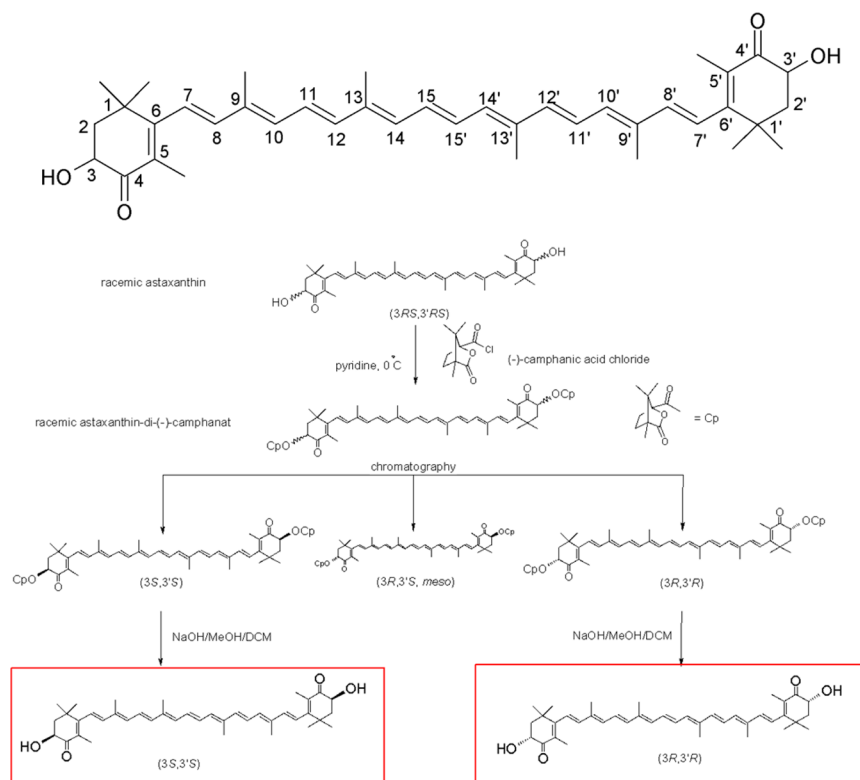


Figure 1. ECD (top) and UV-vis (bottom) spectra of 3R,3'R- and 3S,3'S-astaxanthin. The red vertical dotted line corresponds to the laser Raman excitation wavelength used further for ROA calculations of AXT (commercially available ROA spectrometers are equipped with a 532 nm laser).

while the functional groups modify the spectrum only if they are conjugated to the chromophore. AXT exhibits an intense UV-vis absorption near 500 nm (Figure 1, bottom) typical for most similar carotenoids.

The ECD spectra of the two AXT enantiomers measured in DMSO (Figure 1, top) are mutual mirror images. Several strong ECD bands of alternating sign are present in the UV region of the AXT spectrum, whereas only very weak absorptions can be detected in the visible part. A similar spectral pattern can be observed in the 3S,3'S-astaxanthin ECD spectrum measured in dichloromethane, with a weak negative band at ca. 520 nm (CH_2Cl_2 solution: $\Delta\epsilon = 224 \text{ nm } (+12.8), 249 \text{ nm } (-14.4),$

280 nm (+12.5), 323 nm (−23.1), 384 nm (+6.7), and 521 nm (−3.2)).²⁰ However, no band was observed in the visible region of the ECD spectrum of 3S,3'S-AXT isolated from the *Thraustochytrium* strain (also dissolved in CH_2Cl_2). This is because of the strong absorption in the visible range and comparatively weak CD phenomenon in this very range. This is why the CD data collected from the visible wavelength range are of lower reliability than those registered in the UV range. Moreover, the sign of AXT bands in the visible range of the ECD spectra is likely to be solvent-dependent.

3.2. DFT Calculations and ECD Spectra of AXT Conformers.

3.2.1. Energetics. The energy of the AXT conformers optimized in the gas phase and in DMSO solution strongly depends on the orientation of the end-rings with respect to the polyene chain: the *gauche* conformations are energetically much preferred to the *trans* ones. This seems to be connected to the torsional angles between the rings and the polyene chain. In the *trans* conformers, the chain and the ring double bonds, $\text{C}_7=\text{C}_8$ and $\text{C}_5=\text{C}_6$, are preferred in the *trans* orientation for π -electron delocalization; in the *gauche* conformations, these double bonds are slightly less stabilized by the π -electron delocalization (Scheme 1 and Figure 2). The values of the HOMA aromaticity index can support these observations.^{39–41} These values have recently been shown to be a good measure of the π -electron delocalization: the higher π -electron delocalization, the higher the HOMA index.⁴² Actually, the HOMA indices of the polyene chain extended to C_7-C_6 , $\text{C}_5=\text{C}_6$, $\text{C}_5'-\text{C}_6'$, and $\text{C}_6'=\text{C}_7'$ moieties in the studied AXT conformers indicate that the π -electron delocalization is slightly higher in conformers with *T* conformations and highest for the *TT* conformer (Table S1). Thus, according to the sole π -electron delocalization, the conformer population should have the opposite order.

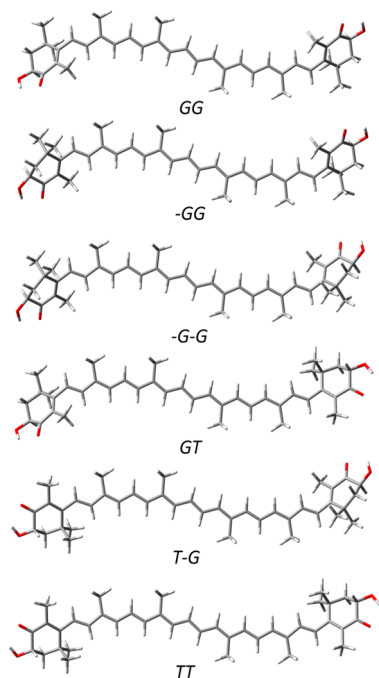


Figure 2. CAM-B3LYP/6-31+G(d,p) PCM-optimized structures of the 3S,3'S-astaxanthin conformers.

So, why is the energetical order of the AXT opposite that suggested by π -electron delocalization? To answer this, one must consider the possible intramolecular repulsions in the studied conformers. Notice that at short distances, the potential curve increases exponentially (or as R^{-12} in the Lennard-Jones potential). Thus, one can expect that with decreasing distance between certain molecular fragments, the repulsion and the conformer energy will increase. The geometry of the all-*E* polyene chain with the attached methyl groups is constant for all set of conformers. The repulsion in the *T* forms is produced by the interaction of the methyl groups of the end rings with

the hydrogen atom at the C₈ or C_{8'} atoms. Overall, we found that the sum of all intramolecular distances between H atoms of the chain C–H and the ring CH₃ groups is a good measure of the repulsion. Indeed, the shorter the distance, the higher the energy of the conformer and thus the higher the repulsion (Figure S1).

3.2.2. ECD Spectra. The results obtained using all DFT functionals indicate that there is a strong dependence of the calculated ECD spectrum on the AXT conformation despite the fact that the AXT end-rings are rather weak chromophores and do not seem to be strongly conjugated to the polyene chain. The differences between the spectra of individual conformers calculated using different functionals but in the PCM model are relatively small (Figure 3). In comparison to that in the gas-phase ECD spectra, the presence of DMSO simulated by using the PCM model results in a red shift of the ECD bands and some minor intensity changes, which are largest for the -GG conformer. These changes are in line with the red shift observed experimentally for both the less polar CH₂Cl₂¹⁹ and the more polar DMSO. The PCM simulation of the CH₂Cl₂ solvent also indicates a red shift of the AXT ECD bands, further increasing for DMSO, i.e., with the increase of the refractive index of the solvent ($n_{\text{DMSO}} = 1.479$, $n_{\text{CH}_2\text{Cl}_2} = 1.424$). On the one hand, one has to bear in mind that the PCM model does not account for the explicit solute–solvent interactions, inter alia, for the H-bonding between AXT containing proton-donating OH groups and DMSO molecules. On the other hand, the main AXT chromophore, the polyene chain, is a nonpolar moiety, and a specific direct H-bonding has a minor influence on this very part of the molecule. For this very reason, the PCM model used here seems to be adequate enough to account for the presence of the solvent despite its polarity.

The experimental and the Boltzmann averaged theoretical ECD spectra of 3S,3'S-AXT in the gas phase and DMSO solution are juxtaposed in Figure 4. The differences in the ECD spectra predicted with different DFT functionals are, first and foremost, due to alterations in the conformer population provided

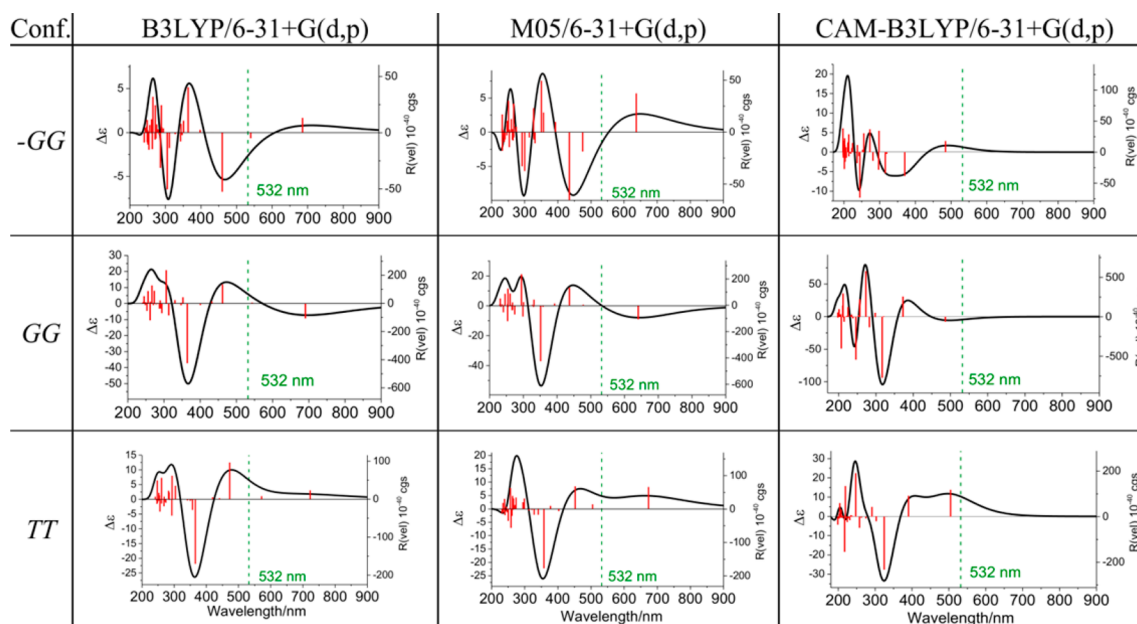


Figure 3. ECD spectra of three selected 3S,3'S-AXT conformers in the DMSO solution calculated at the B3LYP/6-31+G(d,p), M05/6-31+G(d,p), and CAM-B3LYP/6-31+G(d,p) levels.

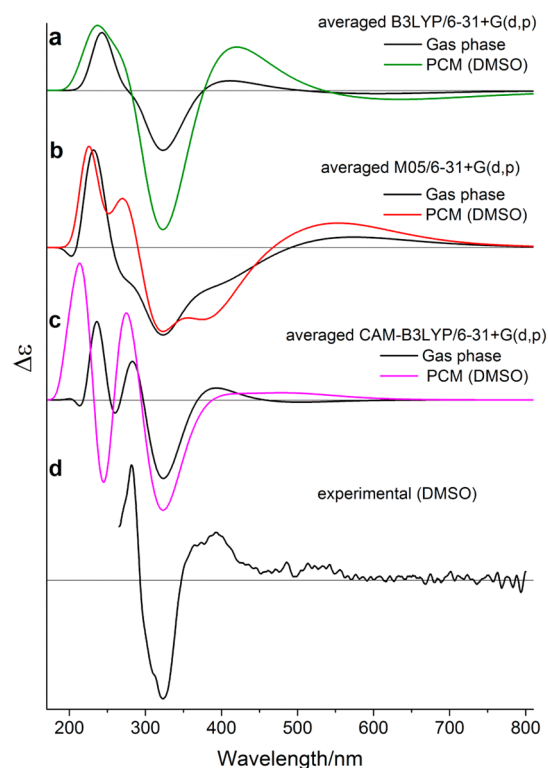


Figure 4. Boltzmann averaged ECD spectra of the 3S,3'S-AXT conformers in the gas phase and DMSO solution simulated by the IEF-PCM model at (a) B3LYP/6-31+G(d,p), (b) M05/6-31+G(d,p), and (c) CAM-B3LYP/6-31+G(d,p) levels, and (d) the experimental ECD spectrum of 3S,3'S-AXT in DMSO. The calculated bands were shifted (scaled) to fit the most intense negative band at ca. 323 nm. The scaling factors are as follows: 0.880 for the B3LYP gas phase, 0.937 for B3LYP PCM; 0.956 for the M05 gas phase, 0.956 for M05 PCM; and 1.092 for the CAM-B3LYP gas phase, 1.010 for CAM-B3LYP PCM.

by the used functionals (Table 1). However, a variation in the predicted ECD band positions and intensities also play a role.

One of the important differences between functionals is the sign of the rotational strength of the first electronic excitation at ca. 600 nm, which is predicted to be positive, negative, and nearly null at the M05, B3LYP, and CAM-B3LYP levels, respectively (Figure 4). The M05 calculated ECD spectrum is in line with our

previous calculations of the ROA spectrum performed for the excitation at 532 nm.²⁷ The conformer averaged preresonance ROA spectrum of AXT obtained with the M05/6-31+G(d,p) method is negative and almost monosigned.²⁷ Nevertheless, for the AXT ROA spectrum, the 532 nm excitation line establishes a preresonance conditions, and the monosigned and negative ROA spectrum is concordant with the prediction of the single electronic-state theory of the RROA spectrum, indicating that the signs of the ECD and ROA spectra must be opposite.⁴³ However, the analogous ROA spectrum calculated at the B3LYP/6-31+G(d,p) level is bisigned, while one would expect it to be monosigned and positive in contrast to the sign of the ECD band at 532 nm predicted by the B3LYP method. This apparent discrepancy is due to a different conformer population causing the population weighted average spectrum of the six nearly monosigned ROA spectra of individual conformers to be bisigned.²⁷

The calculated averaged ECD spectra reproduce well experimental one qualitatively well (Figure 4). The experimental bands are at 281 and 323 nm in all calculated spectra. The most important discrepancy between the calculated and experimental spectra is found at the two ECD bands at ca. 395 and 550 nm. There are two alternative explanations for this discrepancy. The B3LYP and CAM-B3LYP calculations agree with the experimental data, which demonstrates that the band at 394 nm is positive, while it is predicted to be negative according to the M05 calculations. Moreover, the band at ca. 550 nm is positive in the M05 calculations and in the experimental data, while it is predicted to be negative in the B3LYP and ca. null in the CAM-B3LYP calculations (Figure 4). However, one can alternatively attribute the main discrepancies between the theoretical and experimental spectra to inaccuracies in the prediction of band shifts. As such, the B3LYP and CAM-B3LYP predicted ECD spectra are in very good qualitative agreement and there is only one difference in the low-wavelength part of the UV range. Even if this range is of little importance in the context of this study, it seems that agreement with the experimental ECD spectrum is stronger for CAM-B3LYP, especially when the PCM model is applied. Moreover, in the M05 calculated ECD spectra, the negative band at ca. 320 nm is probably split into a doublet, broadened, and red-shifted. In this interpretation, the positive experimental band at ca. 400 nm would be red-shifted toward 550 nm and broadened in the M05 calculations. Nevertheless, good agreement between the ECD spectrum calculated with the CAM-B3LYP PCM functional and the

Table 1. Conformer Population Provided by Used Functionals^a

conf.	sym.	C ₅ =C ₆ -C ₇ =O ₈			C _{5'} =C _{6'} -C _{7'} =O _{8'}			ΔE_{ZPE}			ΔG			population (ΔG)		
		B3LYP	M05	CAM-B3LYP	B3LYP	M05	CAM-B3LYP	B3LYP	M05	CAM-B3LYP	B3LYP	M05	CAM-B3LYP	B3LYP	M05	CAM-B3LYP
GG	C ₂	35.7	40.6	44.4	35.7	40.6	44.4	0.0 ^b	0.2	0.5	0.3	2.7	2.6	14.1	11.8	12.9
-GG	C ₁	-37.4	-41.6	-44.5	35.4	40.2	44.6	0.7	0.0 ^c	0.0 ^d	0.0 ^e	0.0 ^f	0.0 ^g	32.0	71.5	74.9
-G-G	C ₂	-37.4	-41.4	-44.8	-37.4	-41.4	-44.8	1.8	1.1	0.5	3.6	6.6	5.7	3.7	2.5	3.8
GT	C ₁	36.1	41.0	44.2	167.4	162.7	157.0	3.7	5.6	7.0	0.3	4.2	7.1	28.8	13.2	4.3
T-G	C ₁	167.2	162.6	157.8	-38.1	-41.8	-44.6	4.2	6.8	7.0	1.1	10.6	7.3	20.8	1.0	4.0
TT	C ₂	166.9	162.8	157.4	166.9	162.8	157.4	7.6	12.2	14.0	8.5	15.0	17.2	0.5	0.1	0.0

^aTorsional angles (deg), zero-point corrected energies, relative ΔE_{ZPE} (kJ mol⁻¹), and Gibbs free energies ΔG (kJ mol⁻¹) referred to the most stable structure for the studied 3S,3'S-astaxanthin conformers calculated at the M05/6-31+G(d,p), B3LYP/6-31+G(d,p), and CAM-B3LYP/6-31+G(d,p) levels in the PCM model (DMSO). In the Boltzman averaged population analysis (%) at 25°C, Gibbs free energies for all nine possible conformations were taken into account. Percentage value for -GG is the sum of the content of -GG and its equivalent G-G conformer (the same for GT and TG as well as for T-G and -GT). ^b $E_{\text{ZPE}} = -4\,872\,129.32$ kJ mol⁻¹. ^c $E_{\text{ZPE}} = -4\,868\,435.01$ kJ mol⁻¹. ^d $E_{\text{ZPE}} = -4\,869\,518.81$ kJ mol⁻¹. ^e $G = -4\,872\,362.78$ kJ mol⁻¹. ^f $G = -4\,868\,671.16$ kJ mol⁻¹. ^g $G = -4\,869\,751.50$ kJ mol⁻¹.

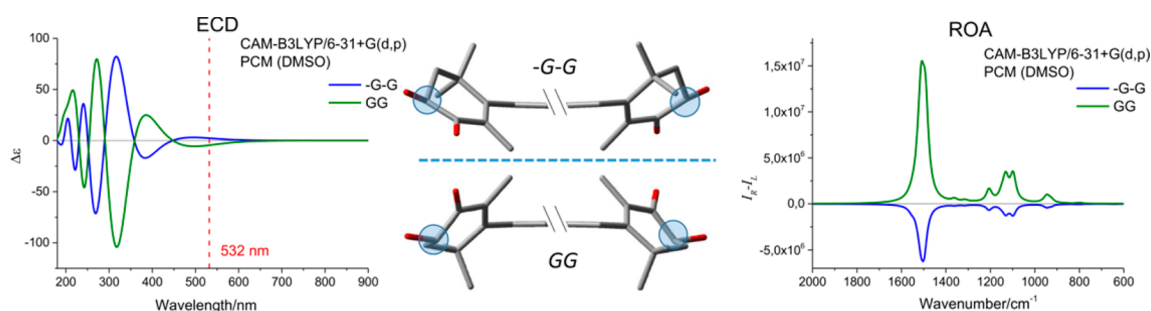


Figure 5. ECD spectra (left panel), molecular structures (middle panel), and ROA spectra (right panel) of $-G-G$ and GG 3S,3'-astaxantin conformers calculated at the CAM-B3LYP/6-31+G(d,p) PCM level of theory.

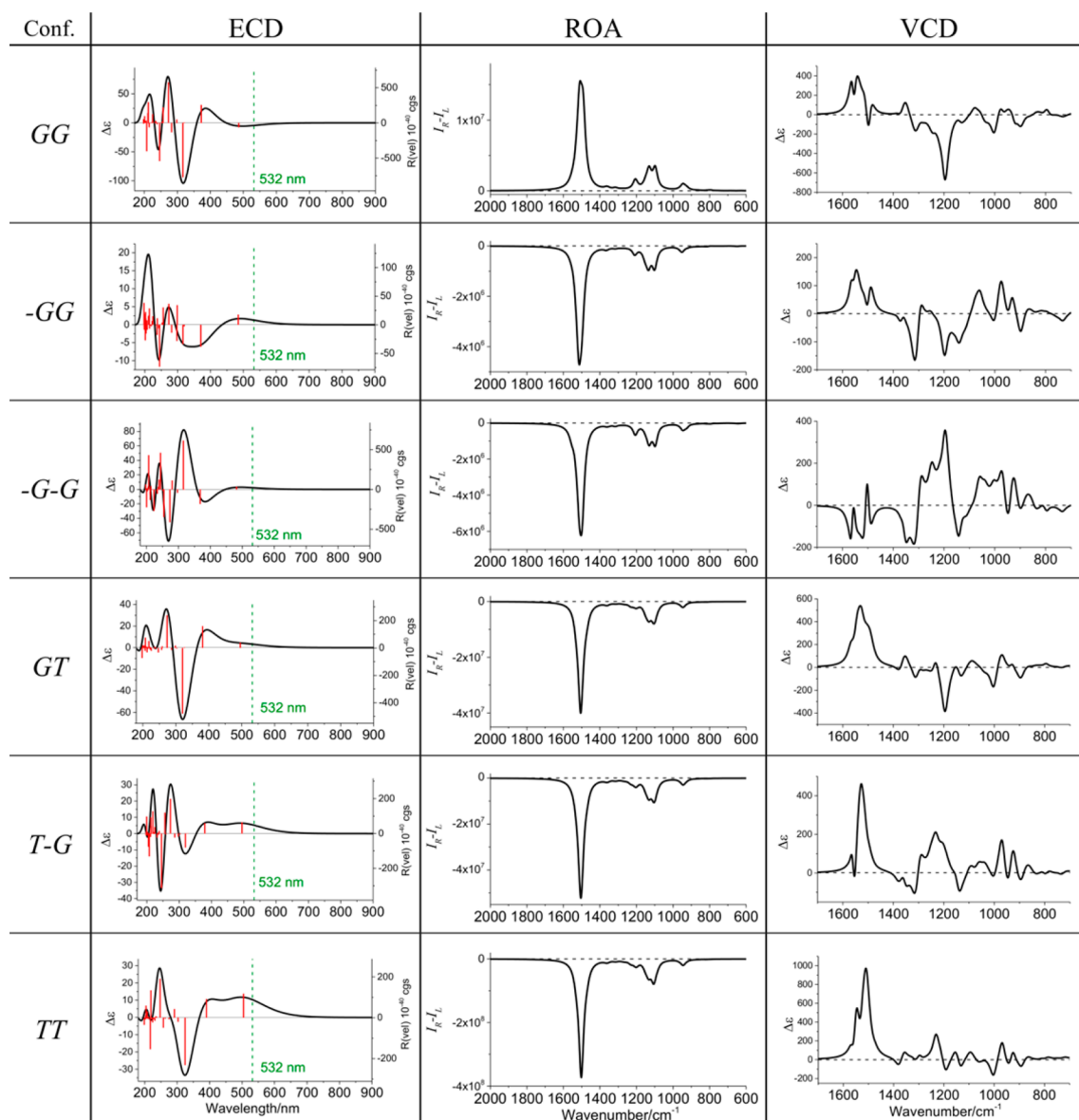


Figure 6. CAM-B3LYP/6-31+G(d,p) PCM calculated ECD, ROA, and VCD spectra of the individual 3S,3'-AST conformers.

experimental spectrum prompted us to base further comparisons on that method (Figure 5 and 6).

3.3. Relationship between ECD and ROA Spectra. First, let us emphasize a rare phenomenon: the calculated ECD and ROA²⁷ spectra of the GG and $-G-G$ 3S,3'-AST conformers are almost mutual mirror images (Figure 5). Recall that GG and $-G-G$ forms are not enantiomers but are simple conformers of

the same enantiomer. Even though the end-rings of these two conformers have the same configuration, their ECD spectra are nearly mutual mirror images. This is because the entire structures are nearly mirror images of each other. Moreover, because the sign of the ECD band at the position of the Raman excitation line (532 nm) determines the sign of the preresonance ROA spectra; the ECD bands of the GG and $-G-G$ 3S,3'-AST

conformers at 532 nm have the opposite sign, and the ROA spectra of GG and -G-G are nearly mirror images too (Figure 5). Furthermore, because the ROA spectra obtained using the 532 nm excitation line are obtained in the preresonance condition, then, according to the single electronic-state RROA theory,^{43,44} they are almost monosigned instead of being bisigned, as in the ordinary nonresonance ROA effect.

There are some unique reports showing the conformers of the same enantiomer manifesting chiroptical spectra (ECD⁴⁵ or ROA⁴⁶) that are nearly mirror images. However, such a close reflection between the two as shown below is truly remarkable (Figure 5).

To further discuss the ROA spectra of astaxanthin, we must clarify two points, especially in the context of our previous paper on theoretical ROA spectra of AXT.²⁷

First, the experimental ROA spectra of AXT can hardly be recorded (the attempts were done with 532 and 780 nm laser excitations). The problem is that the two chiral centers in AXT are too far away from the π -orbital chain for their local stereochemistry to influence the electronic transition of the resonant π -network chain of the molecule. The ROA measurements were performed on a relatively low concentration of AXT compared to those normally used in ROA studies (due to the resonance enhancement of the Raman spectrum of AXT, on the one hand, and its low solubility, on the other), thus leading to a very weak ROA signal. Meanwhile, the resonant Raman signal is very strong, and if there is any small misalignment in the spectrometer (which is very difficult to control), there is a risk of distortions occurring in the ROA spectrum where the largest resonant Raman bands are. This results in an ROA spectrum far weaker than normal (because of the low AXT concentration) and difficult to see against the larger-than-normal distortions resulting from the resonant Raman bands.

Second, one must take into account the limitations of the computing method used here. The Gaussian program allows for computing nonresonant ROA, but the method depends on the frequency of the incident light so one can register some extraneous preresonant effects. This can be explained as follows: ROA intensity differences depend on the normal mode derivatives of three frequency-dependent polarizability tensors (electric dipole–electric dipole (α), electric dipole–magnetic dipole (G'), and electric dipole–electric quadrupole (A)). For resonance ROA, these derivative polarizability tensors are complex (i.e., have both real and imaginary parts). In a far-from-resonance approximation (the Gaussian method used in this work), only the real parts of α and A and only the imaginary

part of G' are computed. One would additionally need the imaginary parts of α and A as well as the real part of G' to correctly treat the resonant case. When the incident frequency is far from an electronic transition, the far-from-resonant approximation is appropriate, as the imaginary parts of α and A (and the real part of G') are very small. As the incident frequency approaches the energy of an electronic transition, the imaginary parts of α and A become large, and their contribution can no longer be neglected. It is therefore not meaningfully efficacious to compute ROA with an incident frequency close to the energy of an electronic transition using the far-from-resonance approximation. Regarding astaxanthin, the value of the first electronic transition calculated (with TD-DFT CAM-B3LYP/6-31+G(d,p) and other previously mentioned functionals) is ca. 600 nm, meaning that our calculated ROA spectra at 532 nm (or 780 nm) are not computed at resonance, and we are recovering some preresonant effects, as discussed in greater detail in our previous paper.²⁷

An important finding from our calculations presented here is the striking difference between either the ECD or the ROA spectra of different conformers (Figure 6). It is worth mentioning that the Raman spectra of these conformers predicted at a similar level of theory are significantly more alike.²⁷ This shows that the two considered chiroptical methods, which manifest considerably different physical phenomena, are very sensitive to slight geometrical differences such as the change from the GG to -GG conformation (Figure 6). Notice that the same conformational change produces almost identical Raman spectra.²⁷

Finally, let us mention the theoretical VCD spectra of the AXT conformers that are juxtaposed with the corresponding ECD and ROA ones (Figure 6). First, notice that the VCD spectra of AXT conformers are always bisigned. This is because, in ROA spectra in preresonance conditions, only the modes connected to the chromophore are very enhanced and much stronger than the other ROA bands. The sign of the preresonance ROA spectra is likely to be determined by the corresponding sign of the ECD band, and therefore, the ROA spectra of these conformers look like their mutual images. At the same time, the VCD spectra are not constrained by any other conditions and are bisigned. Second, in contrast to the ROA spectra, for nearly geometrical mirror image GG and -G-G conformers, the VCD spectra are nearly mutual mirror images only in limited spectral ranges (for example, 1800–1500 cm^{-1} ; Figure 6), whereas in the other spectral ranges (for example, 1300–1100 cm^{-1} ; Figure 6) they are very different. Finally, because the spectral pattern of AXT yielded by VCD is quite independent from that of ROA (and ECD) spectra, it could

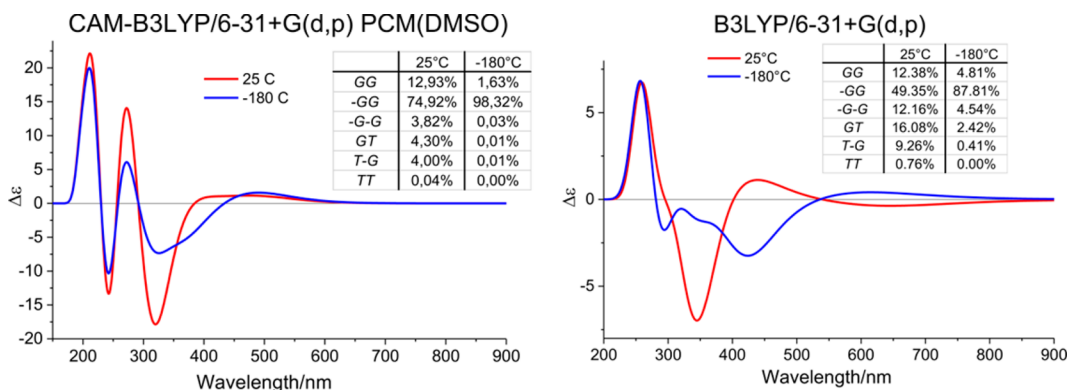


Figure 7. CAM-B3LYP/6-31+G(d,p) PCM (left) and the B3LYP/6-31+G(d,p) (right) calculated ECD spectra of the individual 3S,3S'-AXT conformers at room (25 °C) and liquid nitrogen (−180 °C) temperature.

provide yet another insight into the conformational analysis of the optically active carotenoids.

Moreover, the ECD spectra of 3S,3'S-astaxantin recorded at room temperature and at $-180\text{ }^{\circ}\text{C}$ ²⁵ exhibit strong temperature dependence manifested by a change of sign generating a mirror-image spectrum. To explain this phenomenon, we calculated ECD spectra for all six stable conformers of AXT using various functionals, with and without the PCM model, and compared the population-weighted-average spectra at both temperatures accordingly. The CAM-B3LYP PCM spectra demonstrated dependence on temperature by an alteration only in the intensity of individual bands (Figure 7, left). However, the B3LYP spectra evidently also showed a change of sign leading to the nearly mirror images of the spectrum simulated at room temperature and at $-180\text{ }^{\circ}\text{C}$ (Figure 7, right). On this basis, we suppose that the temperature effect can be connected to the conformational change of AXT toward the G-G conformer (i.e., form having the lowest Gibbs free energy) upon cooling (Figure 7, right). The apparent discrepancy between the results obtained from B3LYP and those using other functionals is related to different conformer populations, which cause the population weighted average spectra of the six ECD spectra to change so significantly.

CONCLUSIONS

The ECD and ROA chiroptical spectra of 3S,3'S-astaxantin conformers were studied by means of DFT calculations using the CAM-B3LYP functional and, as references, B3LYP and M05, combined with the 6-31+G(d,p) basis set and the PCM model. The calculations were supplemented by analyses of the experimental ECD spectra. We found that the M05 functional, which performed well in conformational studies of AXT and previous predictions of the ROA spectrum of AXT at 532 nm excitation,²⁷ seems to be less accurate in reproducing the ECD spectrum of AXT. This is because the ECD bands yielded by M05 are overly red-shifted and broadened. In contrast, the CAM-B3LYP calculations provide an ECD spectral pattern that is in very good agreement with the experimental spectra of AXT, especially when the PCM model is also applied.

Quite unexpectedly, we found that the calculated ECD and ROA spectra of the GG and -G-G AXT conformers are almost mutual mirror images despite the fact that both forms are not enantiomers but rather simple conformers of the same enantiomer. Even though the end-rings of these two conformers have the same configuration, their ECD and ROA spectra are nearly mutual mirror images. In the same time, the VCD spectra of these very conformers display a mirror-image pattern only in limited spectral ranges.

This paper shows some of the potential of chiroptical methods in studying conformational changes of AXT (e.g., due to temperature), even if the optical center is far away from the chromophore groups. The combination of chiroptical spectroscopies, i.e., the ECD and ROA methods, provides information about quite subtle conformational rearrangements of AXT and may make them very attractive for future studies of chiral carotenoids in biological systems.

ASSOCIATED CONTENT

Supporting Information

The Supporting Information is available free of charge on the ACS Publications website at DOI: 10.1021/acs.jpcc.5b07193.

Figures showing the linear correlation between the relative sum of distances between the polyene CH and ring Me

groups and relative energies of the studied conformers; the original, nonscaled Boltzmann averaged ECD spectra of the 3S,3'S-AXT conformers in the gas phase and DMSO solution simulated by the IEF-PCM model at B3LYP/6-31+G(d,p), M05/6-31+G(d,p), and CAM-B3LYP/6-31+G(d,p) levels; and the experimental ECD spectrum of 3S,3'S-AXT in DMSO. Tables showing π -electron delocalization⁴¹ calculated for polyene chains extended to C=C groups of the terminal rings and the CAM-B3LYP/6-31+G(d,p) IEF-PCM (DMSO) optimized geometries of the 3S,3'S-astaxanthin conformers. (PDF)

AUTHOR INFORMATION

Corresponding Author

*E-mail: baranska@chemia.uj.edu.pl. Tel: +48 12 663 22 53.

Notes

The authors declare no competing financial interest.

ACKNOWLEDGMENTS

We express our gratitude to Prof. James Cheeseman (Gaussian, Inc.) and Prof. Ewan Blanch (RMIT University, Australia) for the fruitful discussions and their comments on the work. This work was supported by National Science Center (grant no. DEC- 2012/07/B/ST5/00889). The authors would like to thank the Academic Computer Centre CYFRONET AGH (Krakow, Poland) for their computing time. This research was supported by PL-Grid Infrastructure. We thank Dr. Hansgeorg Ernst from BASF, who kindly supplied us with racemic astaxanthin and 3S,3'S-AXT.

REFERENCES

- (1) Bjerkeng, B.; Berge, G. M. Apparent Digestibility Coefficients and Accumulation of Astaxanthin E/Z Isomers in Atlantic Salmon (*Salmo salar* L.) and Atlantic Halibut (*Hippoglossus hippoglossus* L.). *Comp. Biochem. Physiol., Part B: Biochem. Mol. Biol.* **2000**, *127*, 423–432.
- (2) Østerlie, M.; Bjerkeng, B.; Liaaen-Jensen, S. Plasma Appearance and Distribution of Astaxanthin E/Z and R/S Isomers in Plasma Lipoproteins of Men after Single Dose Administration of Astaxanthin. *J. Nutr. Biochem.* **2000**, *11*, 482–490.
- (3) Matsuno, T.; Maoka, T.; Katsuyama, M.; Ookubo, M.; Katagiri, K.; Jimura, H. The Occurrence of Enantiomeric and meso-Astaxanthin in Aquatic Animals. *Nippon Suisan Gakkaishi* **1984**, *50*, 1589–1592.
- (4) Renström, B.; Borch, G.; Liaaen-Jensen, S. Natural Occurrence of Enantiomeric and meso-Astaxanthin 4. Ex Shrimps (*Pandalus borealis*). *Comp. Biochem. Physiol. B-Biochem. Mol. Biol.* **1981**, *69*, 621–624.
- (5) Østerlie, M.; Bjerkeng, B.; Liaaen-Jensen, S. Accumulation of Astaxanthin all-E, 9Z and 13Z Geometrical Isomers and 3 and 3' RS Optical Isomers in Rainbow Trout (*Oncorhynchus mykiss*) is Selective. *J. Nutr.* **1999**, *129*, 391–398.
- (6) Maoka, T.; Etoh, T.; Kishimoto, S.; Sakata, S. Carotenoids and Their Fatty Acid Esters in the Petals of *Adonis Aestivalis*. *J. Oleo Sci.* **2011**, *60*, 47–52.
- (7) Kaczor, A.; Turnau, K.; Baranska, M. In situ Raman Imaging of Astaxanthin in a Single Microalgal Cell. *Analyst* **2011**, *136*, 1109–1112.
- (8) Renström, B.; Borch, G.; Skulberg, O. M.; Liaaen-Jensen, S. Optical Purity of (3S,3'S)-Astaxanthin from *Haematococcus pluvialis*. *Phytochemistry* **1981**, *20*, 2561–2564.
- (9) Britton, G.; Goodwin, T. W. Carotenoid Chemistry and Biochemistry. In *Proceedings of the 6th International Symposium on Carotenoids*, Liverpool, U.K., 26–31 July 1981; Pergamon Press: New York, 1982.
- (10) Bjerkeng, B.; Følling, M.; Lagocki, S.; Storebakken, T.; Olli, J. J.; Alsted, N. Bioavailability of all-E-Astaxanthin and Z-Isomers of

Astaxanthin in Rainbow Trout (*Oncorhynchus mykiss*). *Aquaculture* **1997**, *157*, 63–82.

(11) Nie, X. P.; Zie, J.; Haubner, N.; Tallmark, B.; Snoeijs, P. Why Baltic Herring and Sprat are Weak Conduits for Astaxanthin from Zooplankton to Piscivorous Fish. *Limnol. Oceanogr.* **2011**, *56*, 1155–1167.

(12) Fleischmann, P.; Baldermann, S.; Yamamoto, M.; Watanabe, N.; Winterhalter, P. Identification, Isolation, and Evaluation of Carotenoid Degradation Enzymes in Japanese Green Tea (*Camellia sinensis*, *Theaceae*). In *State-of-the-Art in Flavour Chemistry and Biology*; Hormann, T.; Rothe, M.; Schieberle, P., Eds; Deutsche Forschungsanstalt für Lebensmittelchemie: Garching, Germany, 2005; pp 234–240.

(13) Coral-Hinostroza, G. N.; Ytrestoyl, T.; Ruyter, B.; Bjerkeng, B. Plasma Appearance of Unesterified Astaxanthin Geometrical E/Z and Optical R/S Isomers in Men given Single Doses of a Mixture of Optical 3 and 3'R/S Isomers of Astaxanthin Fatty Acyl Diesters. *Comp. Biochem. Physiol., Part C: Toxicol. Pharmacol.* **2004**, *139*, 99–110.

(14) Palozza, P.; Krinsky, N. I. Astaxanthin and Canthaxanthin are Potent Antioxidants in a Membrane Model. *Arch. Biochem. Biophys.* **1992**, *297*, 291–295.

(15) Yuan, J. P.; Peng, J.; Yin, K.; Wang, J. H. Potential Health-Promoting Effects of Astaxanthin: A High-value Carotenoid Mostly from Microalgae. *Mol. Nutr. Food Res.* **2011**, *55*, 150–165.

(16) Liu, X.; Osawa, T. Cis Astaxanthin and Especially 9-cis Astaxanthin Exhibits a Higher Antioxidant Activity in vitro Compared to the all-trans Isomer. *Biochem. Biophys. Res. Commun.* **2007**, *357*, 187–193.

(17) Schwartz, S. H.; Qin, X.; Zeevaert, J. A. D. Elucidation of the Indirect Pathway of Abscissic Acid Biosynthesis by Mutants, Genes, and Enzymes. *Plant Physiol.* **2003**, *131*, 1591–1601.

(18) Merlin, J. C. Resonance Raman Spectroscopy of Carotenoids and Carotenoid-containing Systems. *Pure Appl. Chem.* **1985**, *57*, 785–792.

(19) Carmona, M. L.; Naganuma, T.; Yamaoka, Y. Identification by HPLC-MS of Carotenoids of the Thraustochytrium CHN-1 Strain Isolated from the Seto Inland Sea. *Biosci., Biotechnol., Biochem.* **2003**, *67*, 884–888.

(20) Englert, G.; Kienzle, F.; Noack, K. ¹H NMR, ¹³C NMR, UV, and CD. Spectral Data of Synthetic (3S,3'S) Astaxanthin, its 15 cis Isomer, and Some Related Compounds. *Helv. Chim. Acta* **1977**, *60*, 1209–1219.

(21) Andreeva, A.; Apostolova, I.; Velitchkova, M. Temperature Dependence of Resonance Raman Spectra of Carotenoids. *Spectrochim. Acta, Part A* **2011**, *78*, 1261–1265.

(22) Cerezo, J.; Zúñiga, J.; Requena, A.; Ávila Ferrer, F. J.; Santoro, F. Erratum: Harmonic Models in Cartesian and Internal Coordinates to Simulate the Absorption Spectra of Carotenoids at Finite Temperatures. *J. Chem. Theory Comput.* **2014**, *10*, 3586–3587.

(23) Cerezo, J.; Zúñiga, J.; Requena, A.; Ávila Ferrer, F. J.; Santoro, F. Harmonic Models in Cartesian and Internal Coordinates to Simulate the Absorption Spectra of Carotenoids at Finite Temperatures. *J. Chem. Theory Comput.* **2013**, *9*, 4947–4958.

(24) Song, W.; Sun, C.; Yin, W.; Men, Z. Influence of Temperature on the Vibration and Electron Absorption Spectra of all-trans- β -Carotene. *Optik* **2014**, *125*, 6131–6135.

(25) Noack, K. Temperaturabhängiger Circular dichroismus von (3S, 3'R)- und (3S, 3'S)-Adonixanthin. *Helv. Chim. Acta* **1981**, *64*, 1833–1836.

(26) Kaczor, A.; Baranska, M. Structural Changes of Carotenoid Astaxanthin in a Single Algal Cell Monitored in Situ by Raman Spectroscopy. *Anal. Chem.* **2011**, *83*, 7763–7770.

(27) Zajac, G.; Kaczor, A.; Chruszcz-Lipska, K.; Dobrowolski, J. C.; Baranska, M. Bisignate Resonance Raman Optical Activity: A pseudo breakdown of the Single Electronic State Model of RROA? *J. Raman Spectrosc.* **2014**, *45*, 859–862.

(28) Müller, R. K.; Bernhard, K.; Mayer, H.; Rüttimann, A.; Vecchi, M. Beitrag zur Analytik und Synthese von 3-Hydroxy-4-oxocarotinoiden. *Helv. Chim. Acta* **1980**, *63*, 1654–1664.

(29) Yanai, T.; Tew, D. P.; Handy, N. C. A New Hybrid Exchange-Correlation Functional using the Coulomb-attenuating method (CAM-B3LYP). *Chem. Phys. Lett.* **2004**, *393*, 51–57.

(30) Becke, A. D. Density-functional Thermochemistry. I. The Effect of the Exchange-only Gradient Correction. *J. Chem. Phys.* **1992**, *96*, 2155–2160.

(31) Lee, C.; Yang, W.; Parr, R. G. Development of the Cole-Salvetti Correlation Energy Formula into a Functional of the Electron Density. *Phys. Rev. B: Condens. Matter Mater. Phys.* **1988**, *37*, 785–789.

(32) Zhao, Y.; Schultz, N. E.; Truhlar, D. G. Exchange-Correlation Functional with Broad Accuracy for Metallic and Nonmetallic Compounds, Kinetics, and Noncovalent Interactions. *J. Chem. Phys.* **2005**, *123*, 5656–5667.

(33) Laurent, A. D.; Jacquemin, D. TD-DFT Benchmarks: A Review. *Int. J. Quantum Chem.* **2013**, *113*, 2019–2039.

(34) Caricato, M.; Trucks, G. W.; Frisch, M. J.; Wiberg, K. B. Oscillator Strength: How does TDDFT Compare to EOM-CCSD? *J. Chem. Theory Comput.* **2011**, *7*, 456–466.

(35) Brkljača, Z.; Mališ, M.; Smith, D. M.; Smith, A. S. Calculating CD Spectra of Flexible Peptides: An Assessment of TD-DFT Functionals. *J. Chem. Theory Comput.* **2014**, *10*, 3270–3279.

(36) Berova, N.; Polavarapu, P.; Nakanishi, K.; Woody, R. W. *Comprehensive Chiroptical Spectroscopy*, Vol. 1, Chapter 22., Wiley, 2012.

(37) Mennucci, B.; Tomasi, J.; Cammi, R.; Cheeseman, J. R.; Frisch, M. J.; Devlin, F. J.; Gabriel, S.; Stephens, P. J. Polarizable Continuum Model (PCM) Calculations of Solvent Effects on Optical Rotations of Chiral Molecules. *J. Phys. Chem. A* **2002**, *106*, 6102–6113.

(38) Frisch, M. J.; Trucks, G. W.; Schlegel, H. B.; Scuseria, G. E.; Robb, M. A.; Cheeseman, J. R.; Scalmani, G.; Barone, V.; Mennucci, B.; Petersson, G. A.; et al. *GAUSSIAN 09*, Revision D.01; Gaussian, Inc.: Wallingford CT, 2009.

(39) Cyrański, M. K. Energetic Aspects of Cyclic π -Electron Delocalization: Evaluation of the Methods of Estimating Aromatic Stabilization Energies. *Chem. Rev.* **2005**, *105*, 3773–3811.

(40) Kruszewski, J.; Krygowski, T. M. Definition of Aromaticity Basing on the Harmonic Oscillator Model. *Tetrahedron Lett.* **1972**, *13*, 3839–3842.

(41) Krygowski, T. M.; Cyrański, M. K. Structural Aspects of Aromaticity. *Chem. Rev.* **2001**, *101*, 1385–1419.

(42) Dobrowolski, J.; Ostrowski, S. On the HOMA Index of Some Acyclic and Conducting Systems. *RSC Adv.* **2015**, *5*, 9467–9471.

(43) Nafie, L. A. Theory of Resonance Raman Optical Activity: The Single Electronic State Limit. *Chem. Phys.* **1996**, *205*, 309–322.

(44) Vargek, M.; Freedman, T. B.; Lee, E.; Nafie, L. A. Experimental Observation of Resonance Raman Optical Activity. *Chem. Phys. Lett.* **1998**, *287*, 359–364.

(45) Li, X.; Hopmann, K. H.; Hudecova, J.; Isaksson, J.; Novotna, J.; Stensen, W.; Andrushchenko, V.; Urbanova, M.; Svendsen, J. S.; Bour, P.; Ruud, K. Determination of Absolute Configuration and Conformation of a Cyclic Dipeptide by NMR and Chiral Spectroscopic Methods. *J. Phys. Chem. A* **2013**, *117*, 1721–1736.

(46) Li, X.; Hopmann, K. H.; Hudecova, J.; Stensen, W.; Novotna, J.; Urbanova, M.; Svendsen, J. S.; Bour, P.; Ruud, K. Absolute Configuration of a Cyclic Dipeptide Reflected in Vibrational Optical Activity: ab Initio and Experimental Investigation. *J. Phys. Chem. A* **2012**, *116*, 2554–2563.